Technische Universität
ILMENAU

Kissinger, Thomas; James, Stephen W.; Weber, Simone; Mullaney, Kevin; Chehura, Edmond; Pekmezci, Huseyin H.; Barrington, James H.; Staines, Stephen E.; Charrett, Thomas O. H.; Lawson, Nicholas J.; Lone, Mudassir; Atack, Richard; Tatam, Ralph P.

Fibre-optic measurement of strain and shape on a helicopter rotor blade during a ground run: 2. Measurement of shape

Fibre-optic measurement of strain and shape on a helicopter rotor blade during a ground run: 2. Measurement of shape

Thomas Kissinger[1,5] ⦿, **Stephen W James**[1,*] ⦿, **Simone Weber**[4,6], **Kevin Mullaney**[1], **Edmond Chehura**[1], **Huseyin H Pekmezci**[1,7], **James H Barrington**[1], **Stephen E Staines**[1], **Thomas O H Charrett**[1] ⦿, **Nicholas J Lawson**[2,8], **Mudassir Lone**[3,9], **Richard Atack**[4] and **Ralph P Tatam**[1] ⦿

[1] Engineering Photonics, Cranfield University, Bedfordshire MK43 0AL, United Kingdom
[2] National Flying Laboratory Centre, Cranfield University, Bedfordshire MK43 0AL, United Kingdom
[3] Centre for Aeronautics, Cranfield University, Bedfordshire MK43 0AL, United Kingdom
[4] Airbus Helicopters UK Ltd, Kidlington, Oxfordshire OX5 1QZ, United Kingdom

E-mail: s.w.james@cranfield.ac.uk

Abstract
Optical fibre strain and shape measurement sensors were deployed on a rotor blade during a full-speed helicopter ground run, with real-time data wirelessly streamed from rotor hub-mounted sensor interrogators. In part 2 of a 2-part paper series, two-dimensional direct fibre-optic shape sensing (DFOSS), using fibre segment interferometry-based interrogation is investigated. The concept of blade shape change visualisation over one rotation period using rotation displacement surfaces is introduced and the usefulness of DFOSS data to gain additional insights by determining operational modal frequencies independently for both horizontal and vertical vibration directions of the blade is demonstrated.

Supplementary material for this article is available online

Keywords: fibre optic sensors, direct fibre optic shape sensing, shape measurement, helicopter

(Some figures may appear in colour only in the online journal)

---

[5] Now: Institute of Process Measurement and Sensor Technology, Technical University of Ilmenau, PF 100565, 98694 Ilmenau, Germany.
[6] Now: Airbus Helicopters Deutschland GmbH, Industriestrasse 4, 86609 Donauwörth, Germany.
[7] Now: Arm-ECS Research Centre and Centre for Internet of Things (IoT) and Pervasive Systems, University of Southampton, Southampton, SO17 1BJ, United Kingdom.
[8] Now: School of Aerospace, Mechanical and Mechatronic Engineering, The University of Sydney, NSW 2006, Australia.
[9] Now: Lilium GMBH, Munich, Germany.
[*] Author to whom any correspondence should be addressed.

1. Introduction

Shape conveys information about a structure that is easily visualized and interpreted, and its measurement [1, 2] has applications that span medicine [3], robotics [4], aerospace [5] and civil engineering [6]. The capability for shape measurement could also be a key enabling technique for future advances, for example for shape morphing aerospace structures [7–9]. The shape of an object may be deduced indirectly from strain measurements made at strategic locations, processed using strain-deformation retrieval methods [10, 11]. This approach has been explored widely in recent years, including in aerospace applications by organisations such as NASA [11], often using optical fibres as the strain sensing technology. Optical fibres offer a number of advantages compared to standard strain gauges, notably their flexibility, low weight and small dimensions ($\approx$0.13 mm diameter). In addition, optical fibres can be embedded within fibre reinforced composites during fabrication, or can be surface-mounted to facilitate retrofitting. However, indirect shape measurement requires detailed knowledge of the underlying structure to transform the measured strain data into shape information. This could fail through imperfect strain transfer, inaccurate positioning of sensors, the presence of thermal gradients [12], or inaccuracies of the structural model, which could be exacerbated where the structure suffers damage [13].

Direct fibre optic shape sensing (DFOSS) [14–24], has the ability to measure shape directly using an optical fibre/fibre arrangement, allowing the fibre path, and therefore the structure to which the fibre/fibre arrangement is attached, to be followed through space in three dimensions using simple path integration. A major advantage of DFOSS is that it removes the requirement for a detailed structural model of the underlying structure. Since shape is determined directly from within the sensing fibre/fibre arrangement, there is no reliance on external strain transfer from the structure, hence simple surface mounting, even using only adhesive tape, can be sufficient [23].

Existing DFOSS approaches can use standard optical fibre with a single core, e.g. long period gratings (LPGs) [16, 18], or use differential strain measurement in parallel fibre arrangements [14, 15, 17, 19–24]. While LPGs achieve high sensitivities and can offer directional measurements [18], the multiplexing capabilities of LPGs are limited typically to $\approx$10 sensors [25, 26] and they are very sensitive to environmental parameters and thus difficult to use in harsh environments. In contrast to single core approaches, differential-strain based DFOSS systems compare strain measurements made within at least three non-collinear fibre cores with a constant lateral separation, typically measuring strain using fibre Bragg gratings (FBGs) [14, 17, 19, 21] or interferometric sensors [15, 23], but also using Rayleigh [20] or Brillouin scattering [22, 24] approaches. The differential nature of the measurements compensates for the common-mode influence of temperature, often a major limitation in fibre optic sensing due to the high inherent temperature sensitivity of optical fibres. For large structures, interferometric sensors can use longer sensor gauge lengths to acquire the required differential strain information. This results in sensitivities several orders of magnitude larger than can be achieved using scattering or FBG-based sensors, where in the latter the combination of results from hundreds of individual FBGs per metre would be required to compete with the sensitivity of interferometric approaches. Commercially available FBG interrogators based on wavelength-division multiplexing (WDM) typically interrogate $\leqslant$50 FBGs, which leads to low curvature sensitivities particularly on large structures. While optical frequency domain reflectometry (OFDR) can be used to interrogate thousands of FBGs, which has been explored for DFOSS [20, 21], OFDR suffers from even lower strain resolution than WDM-based interrogators. In addition, the OFDR approaches require highly-coherent yet widely-tuneable lasers, which are often mechanically tuned, making systems slow, expensive and difficult to deploy in harsh environments such as helicopter rotor blades.

As shown in Part 1 [27], long-gauge length strain sensors interrogated using our range-resolved interferometry (RRI) signal processing technique [28] offer spatially resolved, fast ($\gg$kHz) and highly sensitive ($\ll$nanostrain$\cdot$Hz$^{-0.5}$) strain measurements using weakly reflecting in-fibre reflectors in an approach termed fibre segment interferometry (FSI) [29], where sensor gauge lengths can range from centimeters [30] to metres [31]. RRI employs an optically simple setup without moving parts, exploiting sinusoidal wavelength modulation through injection-current modulation of robust telecoms distributed feedback laser diodes. The combination of very high sensitivity and the use of robust and cost-effective hardware make interferometric DFOSS based on RRI ideal for use in challenging measurement environments, such as that presented by a rotating helicopter blade.

The present work was carried out within the Innovate UK funded BladeSense (*Measurement of Dynamic Rotor Blade Deformation*) project [32] that aims to investigate the feasibility of the use of advanced strain sensing and DFOSS instrumentation on an Airbus Helicopters H135 blade for providing in-flight measurements to analyse the aerodynamic and aeroelastic properties of the blade, with an ultimate view towards exploring future utility of the measurement techniques for routine in-flight deployment to enable predictive maintenance. The ability of OFS technology to allow the analysis of the vibration characteristics of a rotor blade in a stationary reference frame during a ground vibration test under laboratory conditions has been established previously by the authors [31]. The work presented in this paper is intended as an initial proof of operation of the sensing technology in the rotating frame on a helicopter operating at full rotation speed but without the helicopter taking off. Future projects are planned to develop the instrumentation further for full in-flight use, also involving independent verification measurements that could not be included in the present trial. This paper, the second part of a two part series, details the application of DFOSS to blade deformation sensing. This follows on from Part 1 [27], which instead focuses on the strain sensing aspects of the FSI technology that underpins the DFOSS measurements, comparing the capabilities of the interferometric strain sensing approach with the well-known FBG based strain sensing technology. In this paper, the specific DFOSS sensing

configuration is described before experimental results from the helicopter trials are shown. These results showcase both the quality of the experimental data that can be acquired and provide examples for various possibilities of data visualisation and analysis, including 3D visualisation of blade deformations and spectral data representation. This is followed by a thorough discussion on the limits of the current measurements and possible future improvements, before concluding with a summary and an outlook on the prospects for this technology.

2. DFOSS instrumentation

In this paper, interferometric DFOSS [23] in the rotating frame is demonstrated using a custom-designed interrogation unit. The general setup of the rotor-mounted instrumentation, the wireless data transfer, the technical parameters of the interferometric interrogation unit and FBG-based reflector inscription are detailed in Part 1 [27], while specific aspects relevant to DFOSS are discussed in the following. Figure 1(a) shows the bottom side of the blade with the DFOSS sensing rod attached. When the sensing rod is used for strain analysis, as described in Part 1 [27], signals from all 11 reflectors within the DFOSS sensing rod are evaluated. However, the DFOSS analysis shown here only uses signals from reflector locations 1–7, forming a sensing region with the sensing origin starting $\approx$1.5 m from the rotation axis. The sensing origin is located near the junction of the blade where the blade pitch control cuff merges with the main blade body (see [31] for details), which in this set-up provides the best possible option to serve as the reference point and spatial origin of the DFOSS measurements. This selection of the sensing origin also avoids the pitch control cuff of the blade near the rotor hub and the differing blade cross-section there, which can complicate interpretation of the shape change data. To simplify the certification process for experimental ground testing, the DFOSS sensing rod had to be covered and held in place by the existing helicopter blade protection tape, which is a standard component of the blade. Additionally, the rod was also bonded to the blade using cyanoacrylate adhesive. However, because the blade protection tape does not extend across the whole length of the blade, the position of the distal end of the DFOSS sensing rod was limited to the end of the extent of the blade protection tape coverage, leading to a sensing region of length $\approx$1.2 m. It is hoped that, in future trials, the sensing region could be extended to reach the tip of the blade, as we have previously demonstrated DFOSS measurements of vibration mode shapes along the full-length of a rotor blade in ground vibration tests carried out in the laboratory [31].

In figure 1(b) an annotated photograph of the cross-section of the DFOSS sensing rod is shown. The sensing rod is made from a polylactic acid plastic filament of original diameter 2.85 mm. which was processed to have a D-shaped cross-section, allowing the orientation of the DFOSS sensing rod on the blade surface, and leading to a protrusion height of $\approx$2.5 mm. The fibre strings are inserted into channels cut into the rod material and bonded to the rod using cyanoacrylate adhesive. Here, four fibre strings are arranged in a trapezoidal

pattern, with lateral distances as indicated in the photograph. In each of the four strings A–D, reflectors, formed by low reflectivity FBGs, are located at positions 1–7 as shown in figure 1(a), with adjacent reflectors separated by 190 mm. The phase signals from the interferences between the cleaved fibre tip and the respective reflectors are evaluated to allow the determination of changes in the shape of the blade. In this paper, a nomenclature for the phase signals that consists of the string and reflector location is used, with for example signal A5 corresponding to the interferometric phase signal between the cleaved fibre tip and reflector number 5 in fibre string A. Details of the DFOSS shape calculation algorithm that uses the differential phase signals between different stings can be found in our prior work [23] but the processing steps are also summarised in section 3.3. Originally, in this study, as illustrated in figure 1(b), it was planned to use the differential phase signals $0.5 \cdot \left((Bx - Ax) + (Cx - Dx) \right)$, with x denoting the respective reflector location, for the vertical displacement signal at 1.3 mm lateral separation and differential phase signal $0.5 \cdot \left((Cx - Bx) + (Dx - Ax) \right)$ at the average lateral separation of 1.95 mm for the horizontal displacement signal, resulting in complete orthogonality of the signals. However, due to the fibre breakage in string D described later, this approach could not be used and instead the differential phase signals $(Bx - Ax)$ at 1.3 mm lateral separation were used for vertical signals and $(Cx - Bx)$ at 2.2 mm lateral separation were used to obtain the horizontal signals. Note that because of the small horizontal offset of 0.15 mm between fibre strings A and B, visible in figure 1(b), the second approach unfortunately leads to a small undesired horizontal signal component in the vertical signal. In principle this could be corrected by applying an appropriate rotation matrix to the vertical component, however, since in most cases the vertical blade motions are much larger than the horizontal motions, this is barely noticeable in the signals and no further correction was performed. In future iterations, an improved DFOSS sensor rod layout with completely orthogonal placement, even in case of one fibre failure, would be preferable. Figure 1(c) illustrates the placement of the DFOSS sensing rod on the blade cross section, where it is protected and held in place by the blade protection tape.

As illustrated in figure 1(c), there is a $\approx$9° angle between the nominal blade coordinate system and the coordinate system of the DFOSS sensing rod shown in figure 1(b), where the DFOSS sensing rod coordinate system is used throughout this paper for simplicity. A photograph and dimensions of the custom-designed, robust interferometric interrogation system that was located on the rotor hub is shown in figure 1(d). The instrument can interrogate interferometric phase signals from four optical fibres, each containing 11 reflectors, using 44 real-time processing channels, i.e. interrogate simultaneously 44 interferometers. The data rate for each real-time processing channel is 205 kHz, leading to a maximum interferometric bandwidth (fringe rate) of 100kHz. However, to reduce noise for the experimental trials described in this paper, is was possible to lower the bandwidth to 33 kHz without loss of fringe tracking even while the helicopter was operating at full speed for extended periods. The recorded interferometric phase signals were then down-sampled to a data rate of 3.2 kHz
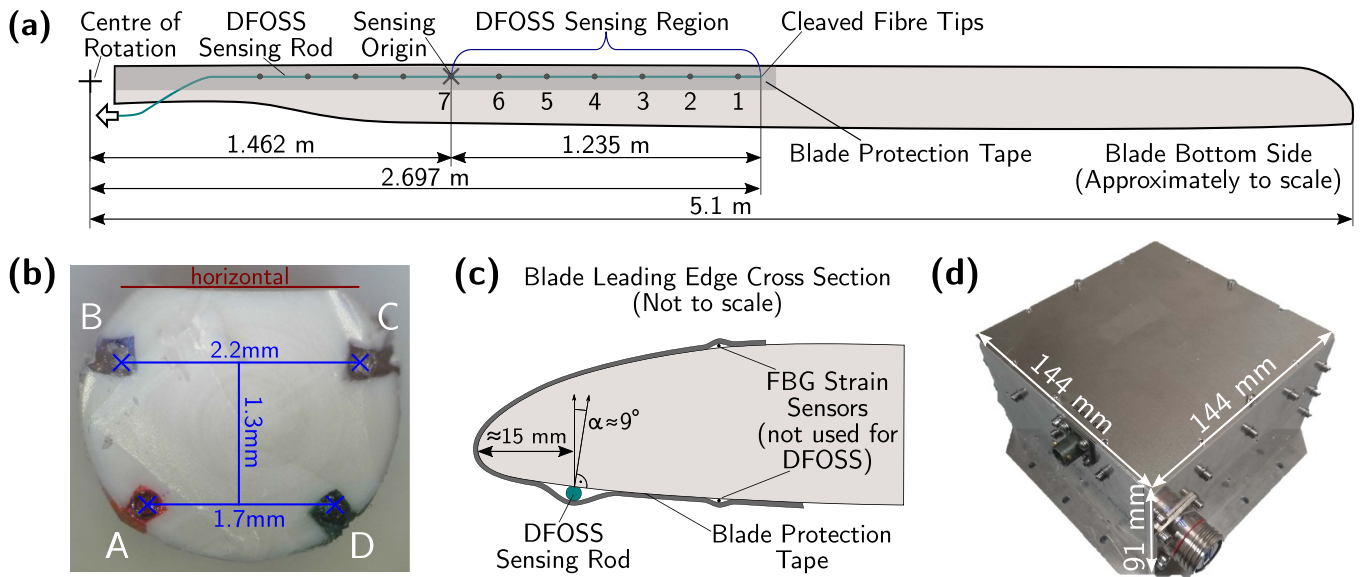
Figure 1. The bottom side of the rotor blade and the configuration of the DFOSS sensing rod are shown in (a) along with a photograph of the rod cross-section in (b), where A, B, C and D denote each of the four optical fibre strings. The placement of the DFOSS sensing rod under the blade protection tape on a cross-section of the blade leading edge is illustrated in (c), while a photograph of the robust interferometric interrogation unit is shown in (d).

by the interrogation unit to lower real-time data rates before transfer to the hub-mounted PC and the subsequent wireless transmission to the ground station, as described in Part 1 [27].

3. Results and discussion

3.1. Test campaign details

The measurement campaign included several individual helicopter operation runs that were carried out sequentially over several days. The individual test runs are detailed in table 1. Here, two short track & balance (T&B) runs were initially performed to adjust and verify the blade balancing. Then a series of three longer measurement runs were performed, with the pilot introducing a predefined series of control inputs onto the helicopter blades, as further detailed in Part 1 [27]. Unfortunately, due to the large mechanical forces experienced during the helicopter operation, what are believed to be microcracks at the grating inscription locations opened in two of the fibre strings during the course of the measurement campaign, blocking fibre transmission and rendering measurements from these fibre strings useless. Furthermore, during T&B Run 1, the first test run overall in the campaign, the wireless connection developed transmission problems during the measurement, allowing only partial recovery of the measurement data.

While for the interferometric strain sensing detailed in Part 1 [27], data from only one fibre string is sufficient, DFOSS requires signals from at least three laterally offset fibre strings. Data from all four fibre strings could only be captured during parts of T&B Run 1, data from three fibre strings could be captured over the entirety of T&B Run 2 and data from all subsequent runs could not be used for DFOSS because less than three fibre strings were available. Therefore, this paper

Table 1. Details of the test campaign.

Run	Length	Working strings	Notes
T&B 1	8 min	A,B,C,D	Partial data capture
T&B 2	5 min	A,B,C	Full data capture
Run 1	24 min	A,C	Full data capture
Run 2	18 min	A,C	Full data capture
Run 3	22 min	A,C	Full data capture

analyses mainly data from T&B Run 2, with the exception of figure 3, where data from a short section of T&B Run 1 that could be recovered is evaluated. The likely origins and future routes for mitigation of fibre breakages are discussed in section 4.

3.2. Raw phase measurements

Figure 2 shows data obtained during T&B Run 2, where figure 2(a) plots the raw phase signals obtained from the interferometers formed between the cleaved fibre end and each of the reflectors, A7–A1, of fibre string A over the complete run. Here, the signals from string A are plotted as an example and the corresponding signals from the other evaluated fibre strings B and C will appear similar when viewed at this scale. As expected, the signal for reflector A7, corresponding to the interferometer with the largest optical path difference, experiences the highest cumulative phase excursion, with those reflectors closer to the cleaved fibre tip experiencing progressively lower phase excursions. Figure 2(b) shows the calculated helicopter rotation rate, which was extracted by evaluating the repetition rate of the characteristic rotation patterns in the phase signals. As the extraction algorithm only worked reliably above 2 Hz, only this data is shown. It can be
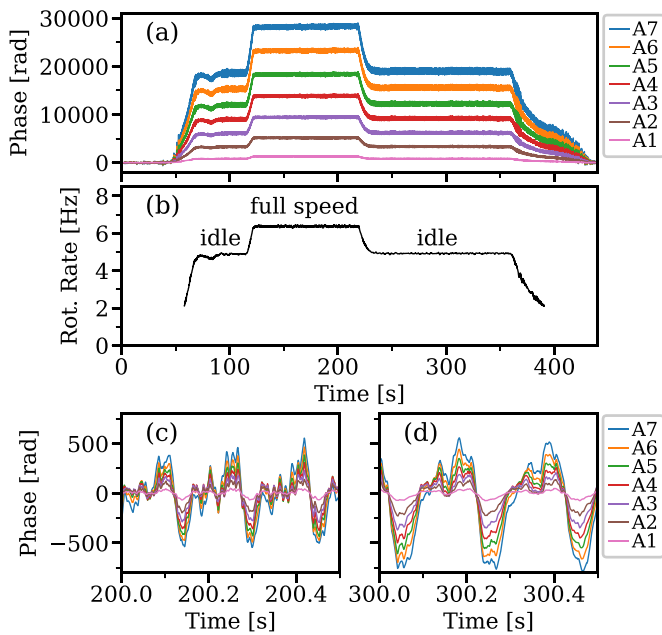
Figure 2. For T&B Run 2, (a) shows the phase signals recorded over the complete run for the interferometers formed between the reflection from the cleaved fibre tip and each of the reflectors, A1–A7, in string A , while (b) displays the extracted helicopter rotation rate (above 2 Hz). (c), (d) Enlarged versions of these phase signals over a period of 0.5 s with their mean removed, with the helicopter being at full speed in (c) and at idle speed in (d).

Figure 3. For T&B Run 1, (a) compares the different phase signals between reflector 7 and the respective fibre tip for all four strings. (b) then plots the vertical differential strain and (c) the horizontal differential strain for reflector 7, in both cases calculated independently from two different fibre string combinations. The secondary *y*-axis shows the equivalent average strain scale for this measurement. Note the different scales between (a) and (b) or (c).

seen figure 2(b) that in the measurement the helicopter was set to idle speed ($\approx$4.9 Hz), then operated at full speed ($\approx$6.4 Hz) for $\approx$100 s, before another idle period and eventual run down. A clear qualitative correspondence to the speed profile as a result of the longitudinal strain due to the centrifugal forces on the blade can be seen in the phase data shown in figure 2(a). Figure 2(c) then shows an enlarged version of the phase signals obtained from string A at full speed, with the mean removed, over a period of 0.5 s, covering approximately three rotation periods. Figure 2(d) enlarges the phase signal during idle speed in a similar fashion. It can be seen in both enlarged plots that signal patterns for each blade rotation are highly complex but broadly repeatable.

Before the DFOSS shape calculations [23] are carried out on the recorded phase signals, it is instructive to look at the differential phase measurements for co-located reflectors, between separate fibre strings. As illustrated in figure 1(b), the difference between signals in fibre strings A, B, C and D can be attributed to vertical and horizontal movement of the DFOSS sensing rod. Furthermore, if signals from all four fibre strings are available, then two signals corresponding to the horizontal and vertical directions can be calculated independently for verification purposes from the two parallel sides of the fibre grid in figure 1(b). As discussed previously, only T&B Run 1 contains usable signals from all four fibre strings. For the section of the measurements with the helicopter running at full speed that could be recovered from T&B Run 1, figure 3 plots the differential phase signals for reflector position 7, i.e. for each string the interference signal between the reflector
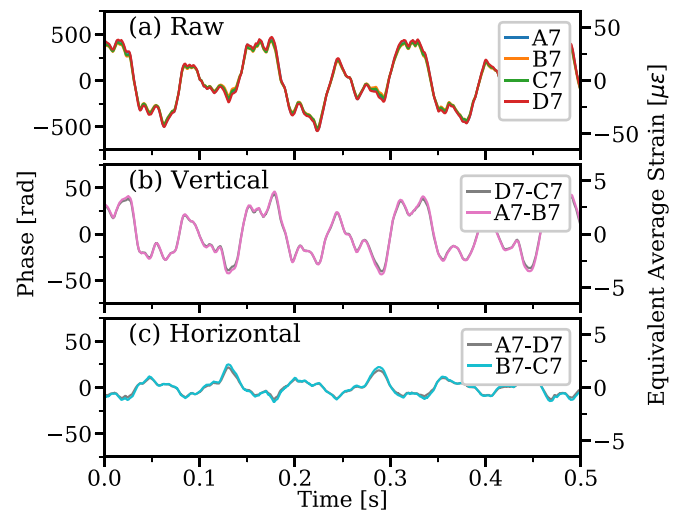
at position 7 and the respective fibre tip (corresponding to a gauge length of 1.235 m) . Figure 3(a) shows a 0.5 s section of the recorded phase signals, corresponding to $\approx$3 rotation periods, for reflectors A7, B7, C7 and D7 with their respective mean removed. It can be seen qualitatively that there is overall agreement between all four measurements. To calculate the vertical differential strain, the difference between reflector signals A7 and B7, or between reflector signals D7 and C7, can be calculated, and the results of these calculations are shown in figure 3(b).

The horizontal differential strain is shown in figure 3(c), calculated independently from the difference between signals B7–C7 and A7–D7. Figures 3(b) and (c) show that the differential strain time traces in the horizontal and vertical directions are distinctly different and further that they both differ significantly from the raw phase signals shown in figure 3(a). Both the vertical and horizontal differential phase signals were acquired using two independent measurements from separate fibre strings, but show a remarkable degree of overlap, giving high confidence in the ability of the system to measure differential strains and indicating the existence of good internal strain transfer within the DFOSS sensing rod. Note that, in general in DFOSS, only internal strain transfer within the rod is necessary for proper operation. External strain transfer between the rod and the structure is not required and the sensing rod merely needs to follow the shape of the structure-under-test [23]. Small scaling differences in the horizontal measurements in figure 3(c) can be expected, due to the different lateral fibre separations of 1.7 mm for signal A7–D7 and 2.2 mm for signal B7–C7. The high measurement quality is evident in these plots with no discernible noise present even when the small differential signals are calculated. For comparison, the secondary *y*-axis in figure 3 is scaled

in equivalent strain units [33] that correspond to the average strain cumulated over the entire ≈1.2 m sensing length, from the cleaved fibre tip to reflector position 7, highlighting the high strain resolutions achievable with this interrogation approach.

3.3. Shape measurements

Results from T&B Run 2 for the overall shape change measurements over the entire DFOSS sensing region are shown figure 4. To obtain the shape data, the recorded phase signals are processed as described in our prior work [23], where the various differential phase signals coupled with information about the lateral fibre string separations yield a discrete set of slope angle measurements for the seven reflector locations. A cubic spline interpolation between reflector locations is then used to obtain a continuous slope angle curve, and subsequent spatial integration yields the vertical/horizontal displacement curves. As discussed previously, the DFOSS measurements are recorded in the reference frame defined by the position and angular orientation of the sensing region origin that is marked in figure 1(a) and the measurements are temporally referenced to the shape of the DFOSS sensing section when the instrument was switched on before helicopter startup, i.e. before the helicopter rotor rotation has started . Here, figure 4(a) shows the vertical blade movements, while figure 4(b) plots the horizontal blade movements, where in both plots the shapes for stationary, idle and full speed operating conditions can be seen. In all cases, the solid line represents the average shape and the shaded regions represent the minimum/maximum shape excursions encountered over a 10 s time period. Here, it can be observed that the maximum shape excursion in the vertical direction approaches 40 mm at the tip of the DFOSS sensing region at ≈2.7 m, while in the horizontal direction, a maximum shape excursion of only ≈8 mm is observed. There are further differences, for example that the vertical measurement in figure 4(a) exhibits very little difference between idle and full speed shapes, i.e. that the blade droop is only minimally reduced between these operating points, while figure 4(b) shows that the horizontal shape excursion is approximately proportional to the rotation speed. For the vertical measurement this is expected because only small changes in the blade coning angle are typically observed between idle and full speed operating conditions. For the horizontal movement this is likely to be caused by an increase in the aerodynamic load on the blade as the rotation speed is increased, leading to a proportional increase in deflection.

To give an indication of the blade winding up, during the transition from stationary to idle operating conditions of the helicopter, the location of the tip of the DFOSS sensing region at a rotor radius of ≈2.7 m, illustrated in figure 1(a), is plotted as a function of rotation angle in the 3D plot in figure 5. Note that the initial position of the helicopter blade is not known and is therefore set arbitrarily to the positive Y direction. It can be seen that the blade height initially winds up very quickly due to the increasing centrifugal forces and then approaches its value at the idle condition more slowly. This experiment demonstrates the feasibility, if the sensing region was to be
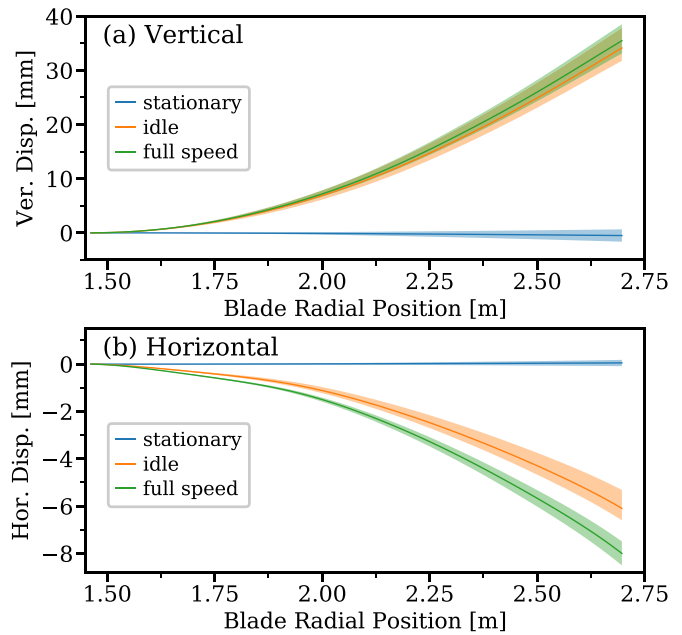

Figure 4. The relative vertical (a) and horizontal (b) displacement over the blade radial position are shown for the stationary, idle and full speed operation of the helicopter. In each plot, the solid line represents the average position, while the shading indicates the minimum/maximum shape excursion, computed over 10 s. Please note the different *y*-axis scales.
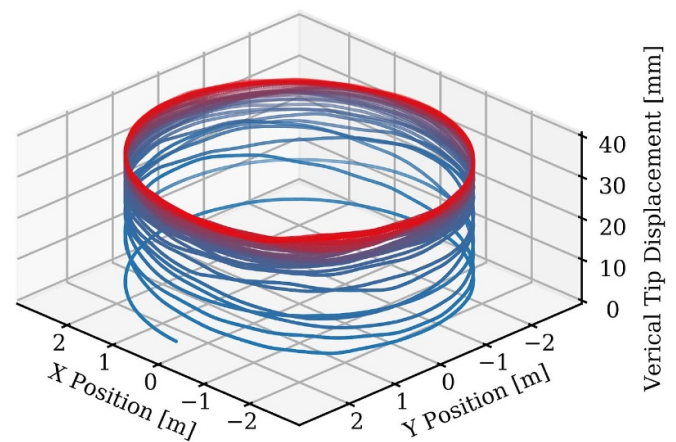

Figure 5. 3D plot of the position of the tip of the DFOSS sensitive region at a rotor radius of ≈2.7 m during the helicopter windup. The line colour has no physical meaning but illustrates the temporal order of data points, with red signifying the most recent data.

extended to the full blade length, of the use of DFOSS to replace or complement existing blade-tip tracking systems. The DFOSS system can provide continuous measurements over the entire rotation period, not just when the blade passes over the fixed sensor/camera location, while also being fully integrated within the blade and therefore immune to environmental conditions.

Measurements of the lateral blade motion orthogonal to the main blade direction are shown in figure 6 by directly plotting vertical against horizontal displacements measured at two locations along the blade. Over a course of a single
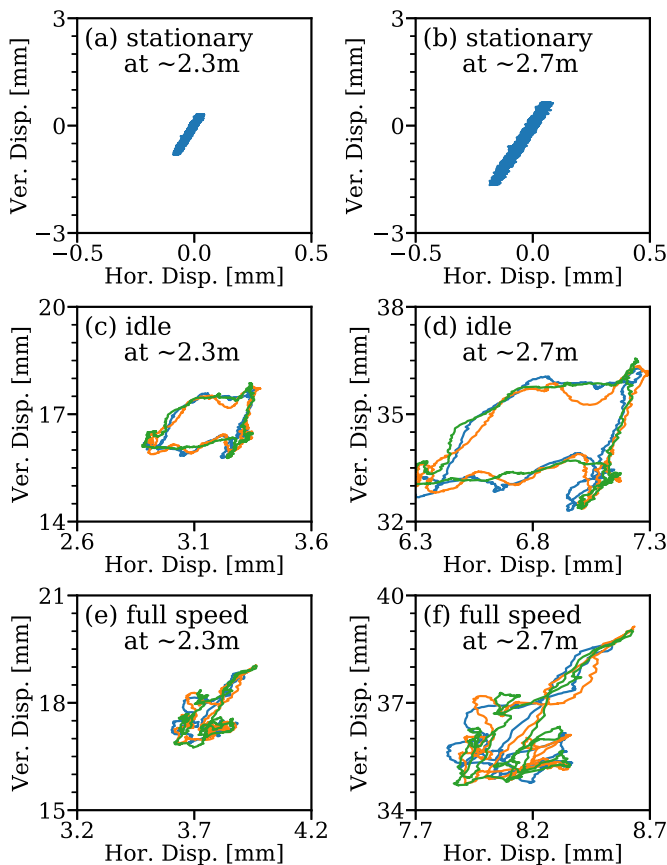
Figure 6. Typical lateral blade motion patterns are illustrated by directly plotting horizontal versus vertical displacement at a rotor radius of ≈2.3 m on the left and ≈2.7 m on the right. (a) and (b) plot the lateral blade movement during the stationary phase, (c) and (d) during the idle operation and (e) and (f) during full speed helicopter operation. Data over a duration of 10 s is plotted in the stationary plots, while in the other plots the three colours signify three consecutive rotation periods. In all plots, note the aspect ratio of 6:1 in the plot scaling.

rotation of the blade, this then results in a characteristic and broadly repeatable motion pattern for each radial rotor position. In figure 6 the plots on the left show this data at a rotor radius of ≈2.3 m and the plots on the right at ≈2.7 m. All plots are displayed with a 6:1 aspect ratio in the scaling to account for the different displacement amplitudes in the vertical and horizontal directions. Figures 6(a) and (b) show this data over a 10 s duration while the helicopter rotor is stationary, where it can be seen that the blade has a preferential motion direction for environment-induced (wind, gusts) natural vibrations. The angle of the motion direction can be determined to be ≈6°, against the vertical direction in the coordinate system of the DFOSS sensor rod. Assuming that the blade vibration is chiefly in the vertical direction in the ground reference frame, this is broadly consistent with the mounting of the DFOSS sensing rod at ≈9° against the blade vertical direction on the blade underside as illustrated in figure 1(c). Figures 6(c) and (d) show the lateral motion data for the helicopter operating at idle speed and figures 6(e) and (f) for full speed operation, where the three colours indicate measurements from three

consecutive rotation periods in order to assess the repeatability of the patterns. Overall, the patterns are distinctly different between idle and full speed operation, but are broadly repeatable for the same operating condition. However, the patterns exhibit local variations between consecutive rotation periods that could be partly caused by varying environmental conditions. It is thought that future research could analyse both the pattern shapes averaged over several revolutions and evaluate the centre-of-gravity of the patterns as a function of rotor position. The logging and observation of any long-term changes could yield a sensitive indicator of the blade health state, as the lateral blade motion shapes and their variations along the blade radius are expected to be dependent on the internal force and mass distribution within the blade and their analysis may provide insight into blade damage and/or water ingress. However, any such advanced analysis is beyond the scope of this paper.

3.4. Rotation displacement surfaces

To gain an insight into the dynamic behaviour of the blade, the visualisation using rotation displacement surfaces is proposed in this paper. These are intended to illustrate the shape *changes* occurring over the course of one revolution and therefore need to have the overall shape excursion removed to be scaled appropriately. To do this, the overall shape excursion is calculated by determining, separately for each rotor radius, the average excursion over many consecutive revolutions. For each rotor radius, this yields a single fixed value that can be subsequently subtracted from the incoming shape data time series at this radius. This process is carried out separately for horizontal and vertical movements. In this paper, to obtain the angular rotor positions, the angles between adjacent zero-crossings of the characteristic rotation patterns, using the same algorithms as in the computation of figure 2(b), are linearly interpolated, however, in future applications the direct use of azimuth angle data from the helicopter rotor would be preferable.

Figure 7 shows the rotation displacement surfaces over one azimuth as a 3D plot, with the rotation plane constituting the *X–Y* plane and the vertical movement perpendicular to this plane. The data for a single revolution of the helicopter at idle operation is shown in figure 7(a) and for the helicopter operating at full speed in figure 7(b). Since the initial position of the helicopter blade is unknown, it is arbitrarily set to the positive X direction. In general, the patterns are broadly repeatable, where in figure 7 the patterns are near continuous at the start and end of the helicopter revolution (red line in figure 7). The high measurement quality of the data is evident in all cases, with features at several angular scales present. For example, the singular feature of higher blade displacement in the vicinity of the positive Y-direction in both plots could be due to an aerodynamic interaction with the helicopter tail. Furthermore, the waviness of the patterns, which is particularly pronounced in the negative Y direction in figure 7(b), shows the complexity of the behaviour of the blade that can be resolved, where further analysis of these patterns is beyond the scope of this
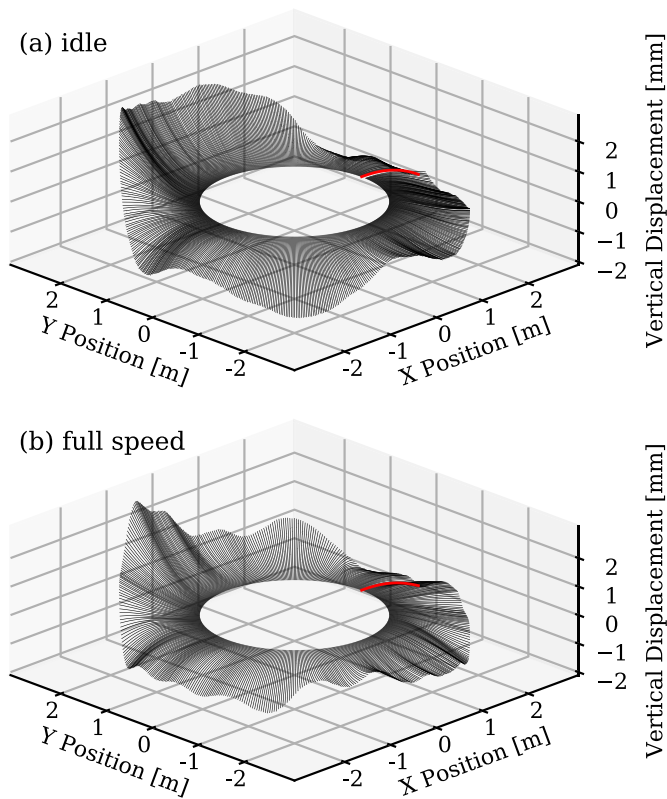
Figure 7. Rotation displacement surfaces for a single rotation in idle (a) and full speed (b) helicopter operation. The first curve lying on the positive X axis is drawn in red and the data is plotted in a anti-clockwise direction.

Figure 8. Rotation displacement surfaces in a colour map representation for a single rotation in idle (left) and full speed (right) helicopter operation, with the vertical data shown in the top graphs and horizontal data in the bottom graphs. A full video sequence of this plot over several rotation periods is available in the supplementary data (available online at stacks.iop.org/SMS/31/075015/mmedia).

paper. It is thought that the use of the information contained in the rotation displacement surfaces could potentially be useful during helicopter operation, for example to visualise the reactions of the blade to dynamic disturbances such as gusts or unusual load conditions, where ultimately the use of this data for automatic control to alleviate disturbances may also be possible.

Figure 8 shows an alternative visualisation of the rotation displacement surfaces using colour maps, based on the same datasets used for figure 7. Here, unlike in the 3D plot representation, the horizontal data in the helicopter rotation plane can be straightforwardly represented. Furthermore, the vertical and horizontal maps in figure 8 are acquired simultaneously, allowing their direct comparison, where, interestingly, the horizontal data in figures 8(c) and (d) shows its furthest excursions in the positive X direction, which is $\approx90°$ offset from the peak excursions for the vertical data. This is expected since the lagging motion lags the flapping motion by $\approx90°$ [34]. In general, particularly in the full speed graphs in figures 8(b) and (d), regular angular patterns indicate the presence of higher order vibration modes.

3.5. Spectral data

Finally, the spectral frequency content of the DFOSS data is analysed in this section, where all shape data used in the following is taken from the tip of the DFOSS sensing region at
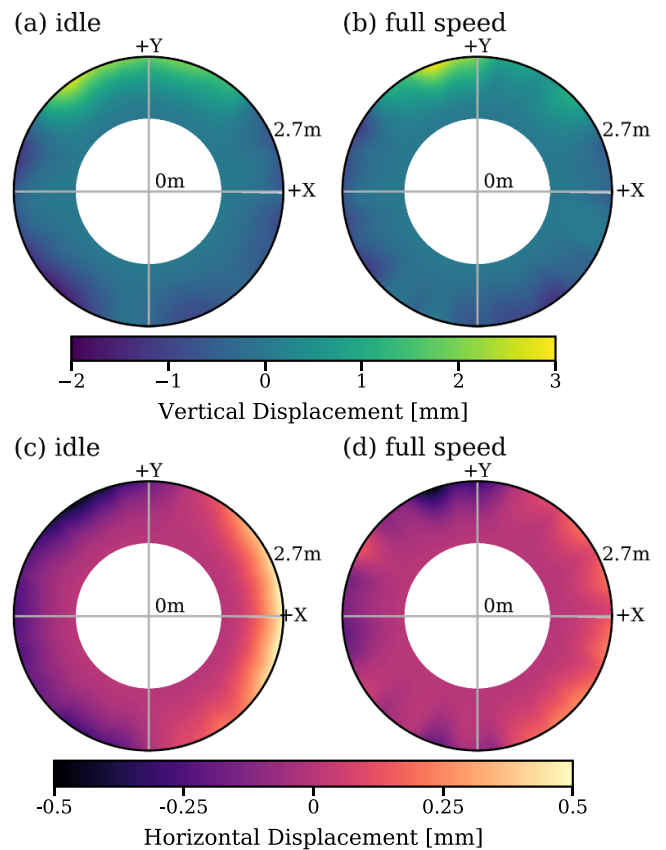
≈2.7 m as illustrated in figure 1(a). A future, more detailed analysis of shape data could also look at differences in the spectral information for varying rotor radii or extract mode shape information, as was already demonstrated for this type of blade in the static frame [31].

In the following, the spectra were computed using Welch's method [35] over 50 s long sections to estimate the power spectral density and then taking the square root of the spectra to yield the displacement amplitude density. The resultant spectra are shown in figure 9 for both vertical and horizontal displacement data, where figure 9(a) shows the spectra for the stationary blade, computed over the first 50 s of the data acquisition. These spectra illustrate that the lower natural blade modes are excited naturally due to ambient wind conditions. In fact, these results i clearly indicate peaks for the first 5 flapping modes at 1.0, 5.4, 15.5, 30.0 and 52.2 Hz. For a detailed discussion of the dynamic characterisation of such rotor blades in the laboratory environment, the reader is referred to [31]. Furthermore, the spectra also demonstrate that the instrument returns a flat displacement amplitude noise floor with a displacement noise density $\approx0.3\ \mu\mathrm{m}\cdot\mathrm{Hz}^{-0.5}$ above 10 Hz, similar for both horizontal and vertical directions. This instrumental noise density agrees well
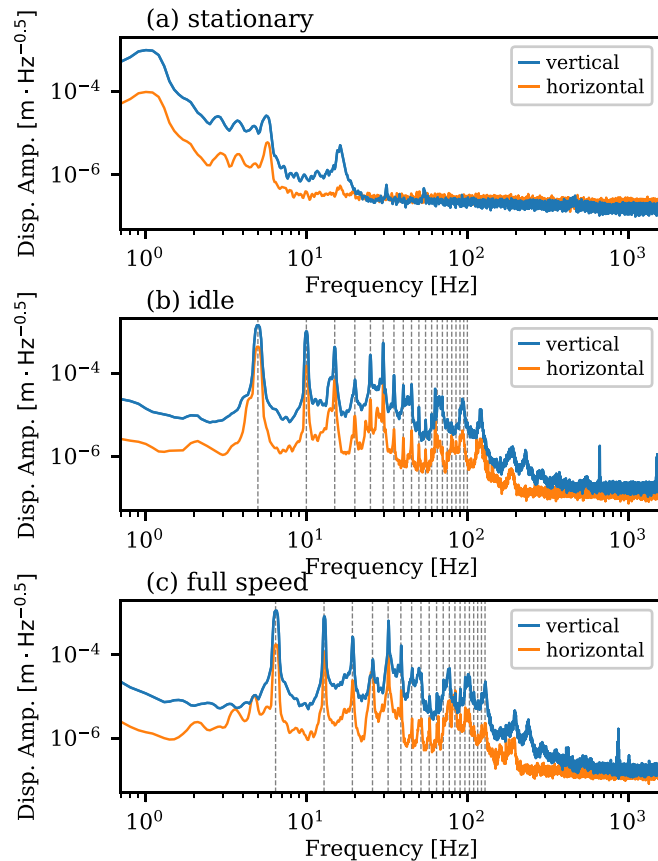
Figure 9. Displacement amplitude density spectra for a stationary helicopter (a) and idle (b) or full speed (c) helicopter operation. The dashed vertical lines mark the first 20 harmonics of the rotation frequency.

with the value of 10 μm for the instantaneous displacement noise standard deviation over the measurement bandwidth of 1.6 kHz, which can be obtained from the same dataset (not shown here). Figure 9(b) plots the spectra for idle helicopter operation, while figure 9(c) plots the spectra for full speed operation. In both cases, the spectra contain a mixture of very sharp peaks due to harmonics of the helicopter rotation frequency as well as broader peaks due to the natural vibration modes of the blade. When comparing horizontal with vertical spectra, it can be seen that in both plots they are broadly comparable but differently scaled. However, the spectra do differ for certain spectral features. For example, the natural mode between 40 and 50 Hz in figure 9(c) is only present in the vertical data but not in the horizontal. Conversely, the weak peaks at ≈3.5 and ≈5 Hz in the same plot are only present in the horizontal data. For modal analysis, this is seen to be a benefit compared to the strain measurements as discussed in Part 1 [27] of this paper series, as it is clearly distinguishable in which direction (vertical or horizontal) the mode signal power contribution is present. Nevertheless, the full identification of the natural modes requires the application of stochastic subspace identification techniques, as was performed in a previous work [31], which is beyond the scope of this paper. In general, the low instrumental noise floor of this DFOSS sensing approach

permits the analysis of even very weakly excited higher order blade vibration modes above 100 Hz.

A further possible means for analysis of the spectral information is through visualisation as spectrograms, as performed in figure 10. First, figures 10(a) and (b) show a time trace of the overall displacement at the tip of the DFOSS sensing region at ≈2.7 m over the complete T&B 2 helicopter run. In both graphs, the insets enlarge a short 0.5 s section during full speed helicopter operation. The corresponding spectrograms are then shown below the respective time traces in figures 10(c) and (d). The spectrograms were computed by taking the logarithm of a short time Fourier transform of the time trace signals. Both figures 10(c) and (d) are scaled with the same dynamic color range but figure 10(d) contains an offset to account for the generally lower amplitudes in the horizontal blade displacements. In both plots, harmonics of the helicopter rotation frequency are clearly visible as sharp lines and scale in direct proportionality to the helicopter rotation frequency. The broader, blade vibration modes can also be clearly identified in the spectrograms. In contrast to the helicopter rotation harmonics, the frequencies of the natural vibration modes show only a small dependence on the helicopter rotation frequencies, where the natural mode shapes generally move to higher frequencies with increasing rotation frequency, due to the increased blade stiffness as a result of the increased centrifugal forces. When comparing figures 10(c) and (d), there are certain natural modes that differ in the two Cartesian directions, for example the excitation of the natural mode at ≈82 Hz at full helicopter speed is visible only in the horizontal spectrogram, while the mode at ≈45 Hz is much more pronounced in the vertical spectrogram. This clearly demonstrates the potential for additional insights into the modal behaviour of the rotor blade that can be gained by independently monitoring both vibration directions using DFOSS. Also, it is interesting to compare the DFOSS spectrograms obtained here with corresponding spectrograms from the strain measurements shown in Part I [27]. Here, it can be seen that in general DFOSS more clearly resolves the natural modes and that simple strain sensing does lack the directional knowledge demonstrated here. Furthermore, it can be seen that by mapping the transitions of the blade vibration frequencies as a function of the helicopter rotation rate, especially visible during wind-down starting at 360 s, it should be possible to acquire the complete Campbell diagram [36] of the helicopter blade, even including weakly excited higher order blade vibration modes. Such analysis could provide useful information for blade characterisation and health monitoring if routinely used.

4. Further discussion

While no direct independent measurement of the blade shape across the sensing region could be acquired in this test, there remains a high degree of confidence in the general validity of the results from our prior body of work [23, 31], where measured displacements and blade vibration characteristics using the DFOSS approach have been successfully verified
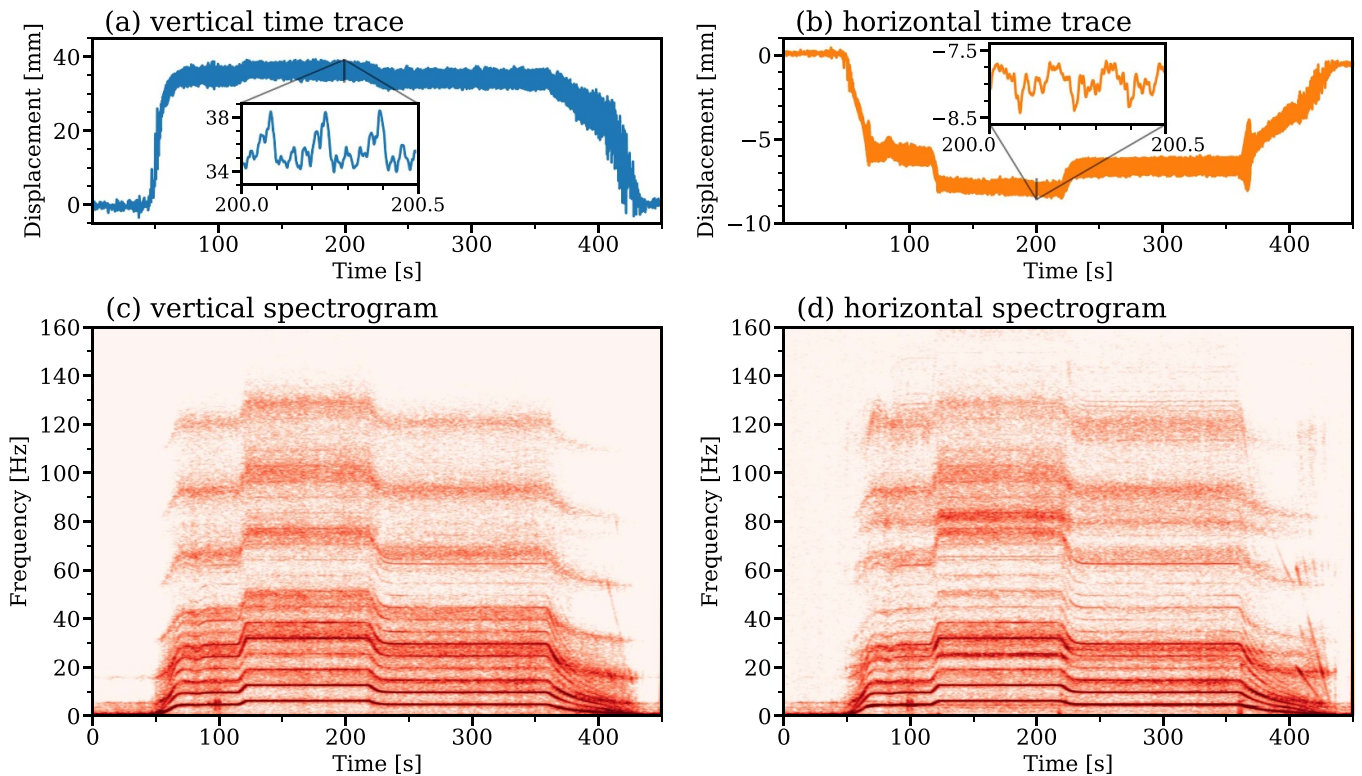
Figure 10. The (a) vertical and (b) horizontal time traces of the displacement at the tip of the DFOSS sensing region at ≈2.7 m is shown, with the insets enlarging a 0.5 s section at full speed helicopter operation. The spectrograms in logarithmic colour scaling are shown in (c) and (d) directly below their respective time trace.

using independent measurements in a static environment. Due to the high linearity of fibre optic strain measurements over large strain ranges [37], the large centrifugal forces present in this test are not expected to significantly affect DFOSS measurement fidelity. A further point that could affect the accuracy of the DFOSS experiment was the assumption of negligible blade twist, as the current DFOSS system cannot resolve this. In this work, the helicopter blade was deemed to be sufficiently rigid to justify this assumption. Ultimately, only a future research project can provide complete certainty of the performance validating the outcome with independent on-rotor measurements, such as camera systems [38]. However, the present study serves as a useful proof-of-principle experiment to explore the capabilities of this approach, and no detrimental effects on the measurement fidelity due to the helicopter rotation were observed here. The evaluation of both horizontal and vertical displacement spectra and the analysis of their differences demonstrates is a key distinguishing feature of the proposed DFOSS sensing approach, where this kind of directional vibration information would be significantly more difficult to obtain with regular strain sensors, such as strain gauges. Moreover, the material properties of the underlying structure do not need to be known to infer shape [31].

A further key aspect that greatly influences the accuracy of the measurements is the choice of sensing origin that defines the reference frame in all six degrees of freedom for the DFOSS measurement. If there are motion-induced changes in the position or angular orientation of the sensing origin relative to the rotor reference frame, then additional motion data or

post-processing steps to transform the data into the desired reference frame might be necessary [31]. However, for usage of the measurements for dynamic characterisation, such as blade operational modal frequency analysis and in-service fatigue monitoring or vibration-based damage detection, these accuracy considerations may only be of secondary importance. For these applications, the current approach of placing the sensing origin on the blade could be directly used in-service. Otherwise, if knowledge of the blade shape changes are required, it would be preferable to place the sensing origin on the blade root or even the rotor hub itself.

The current DFOSS implementation can provide only shape measurements relative to the shape at instrument start-up. As a result, there is no information on the initial shape of the blade. Also, in extreme circumstances, a temporary loss of tracking of the interferometric phase signal could occur that would lead to a persistent shape tracking error. Again, for certain applications that require only dynamic data, such as the analysis of spectral data and the proposed rotation displacement surfaces, solely using relative data, even with the possibility of tracking errors, this is of little concern. However, for some applications absolute shape measurements, which would provide the initial shape data and avoid the possibility of tracking errors, may be required. Such absolute measurements could be provided, for example, by a future advanced DFOSS implementation using a two-wavelength interferometric approach [39]. It is also important to note that the present DFOSS approach does not suffer from integration and drift errors that commonly affect inertial sensors, as

only phase tracking is performed- there is no integration of temporal derivative data. Furthermore, unlike measurement approaches using accelerometers, the DFOSS approach is completely immune to the overall helicopter motion and does not require post-processing to estimate and remove the signals corresponding to the helicopter rotational and translational motion.

A further possible future improvement would involve the use of multi-core fibres (MCF), where in an MCF several fibre cores are integrated within a single optical fibre. For example, four-core MCF with a lateral core spacing of 50 μm is now commercially available. The primary advantages of using MCF are their low weight and their small cross section (down to 0.13 mm), potentially allowing direct embedding within the blade composite structure. Disadvantages are the reduced displacement sensitivity, which in DFOSS scales inversely with the lateral core displacement [23], leading to a reduction in displacement sensitivity compared to the present implementation by a factor of ≈30 to 50. However, based on the measurement resolutions achieved here, sub-millimetre blade tip displacement resolutions at kHz data rates still seem feasible using MCF with the current DFOSS approach. A further challenge with the use of MCF is maintaining a consistent fibre orientation, which must remain identical with reference to the blade surface along the whole sensing length. However, recent developments, such as the use D-shaped MCF [24] or flat MCF [40], could be a feasible way to solve the MCF orientation challenge.

During the measurement campaign two fibre strings developed faults, where in one instance the fault could be observed in the measurements and occurred during a period at full helicopter speed where a strong blade load was applied through a pilot input. After the tests, the fibres were assessed using a Luna optical backscatter reflectometer and, in both fibre strings, a region of high loss was found to be localised at the location of a particular grating where the polyacrylate coating of the fibre had been stripped during grating production. Through movement of the blade droop to the original state during sensor adhesion, fibre transmission could be reinstated, leading to the conclusion that micro-cracks have developed at the grating reflector locations, which open and close depending on the blade load. Optical fibres, in their as-manufactured state with their polymer protective buffer jacket intact, have a high intrinsic tensile strength, with a breaking strain of approximately 6%, but removal of the coating from the fibre by mechanical means can induce surface flaws and cracks that reduce the strength of the fibre. It is thought that the application of the grating reflectors without coating in this study weakened the fibre, causing the observed failures. These effects can be readily mitigated though improved reflector production methods. It is possible to use FBGs that are written on the draw tower, immediately after the fibre has been manufactured and before a protective coating is applied, retaining the full tensile strength of the fibre [41]. It is also possible, using femtosecond lasers, to fabricate FBGs through the coating of the fibre [42]. Finally, UV-written FBGs can be re-coated with a polymer buffer jacket to increase the localised strength of the fibre. It is also stressed here that throughout the entire measurement

campaign, the interferometric interrogation unit of figure 1(d) remained fully functioning over a combined helicopter operating time of more than one hour and continues to operate.

5. Conclusions

A novel interferometric direct DFOSS technique for measuring blade deformations has been tested in the rotating frame on a helicopter operating at full rotation speed of 6.6 Hz. The rotor-mounted interrogation system can measure independently blade displacements in the two Cartesian directions perpendicular to the DFOSS sensing rod, which has a protrusion diameter of ≈2.5 mm and was surface mounted onto the blade. Over the sensing region of ≈1.2 m, measurements with a displacement noise standard deviation of ≈10 μm at a data rate of 3.2 kHz in both Cartesian directions could be acquired. This data could be analysed in a number of ways. For example, it was shown that it could be used for blade tip motions and for the direct visualisation of lateral blade motions perpendicular to the sensing rod, which may give insight into the health of the blade. The proposed 'rotation displacement surfaces' concept also shows promise for instantaneous visualisation of dynamic blade shape deformations occurring over one blade revolution. Furthermore, the spectral analysis of the data, particularly when information from the simultaneous and spatially co-located acquisition of two Cartesian dimensions is employed, was shown to resolve many of the natural modes present.

The high sensitivity of the interferometric approach, which far exceeds comparable techniques based on electrical or fibre-optic strain gauges, and the immunity to helicopter rotational motion effects and instrument drift, which distinguishes the concept from accelerometer measurements, have been demonstrated. Future investigations could improve on this experiment, for example taking it to full flight operation, or by providing absolute shape information that can recover the blade shape at any instant, without the commonly adopted blade tip tracking techniques. Furthermore, the use of MCF that could be directly embedded into the blade is very attractive and it is thought that currently only interferometric DFOSS is sensitive enough to provide sub-millimetre displacement resolution when used within a MCF instrumented blade.

ORCID iDs

Thomas Kissinger https://orcid.org/0000-0003-1832-7143
Stephen W James https://orcid.org/0000-0003-0651-9842
Thomas O H Charrett https://orcid.org/0000-0002-6677-7264
Ralph P Tatam https://orcid.org/0000-0001-9599-3639

References

[1] Amanzadeh M, Aminossadati S M, Kizil M S and Rakić A D 2018 Recent developments in fibre optic shape sensing *Measurement* **128** 119–37

[2] Floris I, Adam J M, Calderón P A and Sales S 2021 Fiber optic shape sensors: a comprehensive review *Opt. Lasers Eng.* **139** 106508

[3] Roesthuis R J, Kemp M, van den Dobbelsteen J J and Misra S 2013 Three-dimensional needle shape reconstruction using an array of fiber Bragg grating sensors *IEEE/ASME Trans. Mechatronics* **19** 1115–26

[4] Ren H, Shi C, Najdovski Z, Fukuda T, Li T, Qi P, Luo X and Song S 2016 Shape sensing techniques for continuum robots in minimally invasive surgery: a survey *IEEE Trans. Biomed. Eng.* **64** 1665–78

[5] Gherlone M, Cerracchio P and Mattone M 2018 Shape sensing methods: review and experimental comparison on a wing-shaped plate *Prog. Aerosp. Sci.* **99** 14–26

[6] Wu H, Guo Y, Xiong L, Liu W, Li G and Zhou X 2019 Optical fiber-based sensing, measuring and implementation methods for slope deformation monitoring: a review *IEEE Sens. J.* **19** 2786–800

[7] Tomić Mš C, Djinović Z V, Scheerer M and Petricevic S J 2018 Measurement of morphing wing deflection by a cross-coherence fiber optic interferometric technique *Smart Mater. Struct.* **27** 015017

[8] Liu Y, Du H, Liu L and Leng J 2014 Shape memory polymers and their composites in aerospace applications: a review *Smart Mater. Struct.* **23** 023001

[9] Barbarino S, Saavedra Flores E I, Ajaj R M, Dayyani I and Friswell M I 2014 A review on shape memory alloys with applications to morphing aircraft *Smart Mater. Struct.* **23** 063001

[10] Rapp S, Kang L H, Han J H, Mueller U C and Baier H 2009 Displacement field estimation for a two-dimensional structure using fiber Bragg grating sensors *Smart Mater. Struct.* **18** 25006

[11] Nicolas M J, Sullivan R W and Richards W L 2016 Large scale applications using FBG sensors: determination of in-flight loads and shape of a composite aircraft wing *Aerospace* **3** 18

[12] Burnett J G, Blanchard P M and Greenaway A H 2000 Optical fibre-based vectoral shape sensor *Strain* **36** 127–33

[13] Loutas T H and Bourikas A 2017 Strain sensors optimal placement for vibration-based structural health monitoring. The effect of damage on the initially optimal configuration *J. Sound Vib.* **410** 217–30

[14] Gander M J, MacPherson W N, McBride R, Jones J D C, Zhang L, Bennion I, Blanchard P M, Burnett J G and Greenaway A H 2000 Bend measurement using Bragg gratings in multicore fibre *Electron. Lett.* **36** 120–1

[15] Blanchard P M *et al* 2000 Two-dimensional bend sensing with a single, multi-core optical fibre *Smart Mater. Struct.* **9** 132–40

[16] Ye C C, James S W and Tatam R P 2000 Simultaneous temperature and bend sensing with long-period fiber gratings *Opt. Lett.* **25** 1007–9

[17] Flockhart G M H, Macpherson W N, Barton J S, Jones J D C, Zhang L and Bennion I 2003 Two-axis bend measurement with Bragg gratings in multicore optical fiber *Opt. Lett.* **28** 387–9

[18] Allsop T, Gillooly A, Mezentsev V, Earthgrowl-Gould T, Neal R, Webb D J and Bennion I 2004 Bending and orientational characteristics of long period gratings written in D-shaped optical fiber [directional bend sensors] *IEEE Trans. Instrum. Meas.* **53** 130–5

[19] Macpherson W N, Barton J S and Moore A J 2006 Tunnel monitoring using multicore fibre *Meas. Sci. Technol.* **17** 1180

[20] Duncan R G, Froggatt M E, Kreger S T, Seeley R J, Gifford D K, Sang A K and Wolfe M S 2007 High-accuracy fiber-optic shape sensing. In sensor systems and networks conf. 2007 *Proc. SPIE* **6530** 65301S

[21] Moore J P and Rogge M D 2012 Shape sensing using multi-core fiber optic cable and parametric curve solutions *Opt. Express* **20** 2967–73

[22] Zhao Z, Soto M A, Tang M and Thévenaz L 2016 Distributed shape sensing using Brillouin scattering in multi-core fibers *Opt. Express* **24** 25211–23

[23] Kissinger T, Chehura E, Staines S E, James S W and Tatam R P 2018 Dynamic fiber-optic shape sensing using fiber segment interferometry *J. Lightwave Technol.* **36** 917–25

[24] Zafeiropoulou A, Masoudi A, Zdagkas A, Cooper L and Brambilla G 2020 Curvature sensing with a D-shaped multicore fibre and Brillouin optical time-domain reflectometry *Opt. Express* **28** 1291–9

[25] Koyama O, Sumiana H, Toyooka Y and Yamada M 2013 High temperature detection inside large-scale plants using distributed sensor fabricated by 10 LPG resonant wavelengths multiplexing *IEICE Electron. Express* **10** 20130586

[26] Murphy R P, James S W and Tatam R P 2007 Multiplexing of fiber-optic long-period grating-based interferometric sensors *J. Lightwave Technol.* **25** 825–9

[27] James S W *et al* 2022 Optical fibre sensors deployed on a helicopter rotor blade during a ground run: 1. Measurement of strain *Smart Mater. Struct.* accepted (https://doi.org/10.1088/1361-665X/ac736d)

[28] Kissinger T, Charrett T O H and Tatam R P 2015 Range-resolved interferometric signal processing using sinusoidal optical frequency modulation *Opt. Express* **23** 9415–31

[29] Kissinger T, Correia R N G, Charrett T O H, James S W and Tatam R P 2016 Fiber segment interferometry for dynamic strain measurements *J. Lightwave Technol.* **34** 4620–26

[30] Aime L F J, Kissinger T, James S W, Chehura E, Verzeletti A and Tatam R P 2021 High sensitivity pressure measurement using optical fibre sensors mounted on a composite diaphragm *Opt. Express* **29** 4105

[31] Weber S *et al* 2021 Application of fibre optic sensing systems to measure rotor blade structural dynamics *Mech. Syst. Signal Process.* **158** 107758

[32] Weber S *et al* 2018 Bladesense—a novel approach for measuring dynamic helicopter rotor blade deformation *44th European Rotorcraft Forum (ERF) 2018 (Delft, The Netherlands)* p 170

[33] Kissinger T, Charrett T O H and Tatam R P 2013 Fibre segment interferometry using code-division multiplexed optical signal processing for strain sensing applications *Meas. Sci. Technol.* **24** 094011

[34] Bramwell A R S, Done G and Balmford D 2001 *Bramwell's Helicopter Dynamics* 2nd edn (Oxford: Butterworth-Heinemann)

[35] Welch P D 1967 The use of fast Fourier transform for the estimation of power spectra: a method based on time averaging over short, modified periodograms *IEEE Trans. Audio Electroacoust.* **15** 70–73

[36] Rammer R, Priems M and Konstanzer P 2013 Modification of a four bladed main rotor—impact on dynamics and vibrations *39th European Rotorcraft Forum, (Moscow, Russia, 3–6 September 2013)* pp 1–10

[37] Jülich F, Aulbach L, Wilfert A, Kratzer P, Kuttler R and Roths J 2013 Gauge factors of fibre Bragg grating strain sensors in different types of optical fibres *Meas. Sci. Technol.* **24** 094007

[38] Boden F, Stasicki B and Ludwikowski K 2018 Optical rotor-blade deformation measurements using a rotating camera *38th European Test and Telemetry Conf. (Nuremberg, Germany)* pp 147–54

[39] Polhemus C 1973 Two-wavelength interferometry *Appl. Opt.* **12** 2071–4

[40] Zafeiropoulou A, Masoudi A, Cooper L and Brambilla G 2021 Flat multi-core fibre for twist elimination in distributed curvature sensing *Opt. Fiber Technol.* **66** 102663

[41] Askins C G, Putnam M A, Patrick H J and Friebele E J 1997 Fibre strength unaffected by on-line writing of single-pulse Bragg gratings *Electron. Lett.* **33** 1333–4

[42] Martinez A, Khrushchev I Y and Bennion I 2006 Direct inscription of Bragg gratings in coated fibers by an infrared femtosecond laser *Opt. Lett.* **31** 1603–5